Check for updates

Stabilizing Nickel-Rich Cathodes in Aqueous Process through Nanocellulose as Water Barrier

Ying Wang, Ying Fang, Luyao Huang, Jiwei Wang, Hua Zhou, Guanyi Wang, Qingliu Wu, Guofeng Wang, and Hongli Zhu**

Nickel-rich $LiNi_{0.8}Co_{0.1}Mn_{0.1}O_2$ (NMC 811) cathode offers high voltage and high specific capacity, making it promising for high energy density batteries. However, large-scale manufacturing of aqueous-processed NMC 811 electrodes remains challenging due to proton exchange causing material decomposition and capacity loss. This work addresses this issue by constructing an in situ nanocellulose protective layer for NMC 811 particles via electrostatic interactions during the slurry preparation. For the first time, the interatomic spacing between inter-chains of nanocellulose is measured through wide-angle X-ray scattering and demonstrate the ability to effectively confine interlayer water using atomistic simulations. Moreover, this nanocellulose coverage simultaneously minimizes Li^+ surface segregation and mitigates water infiltration. Owing to less material decomposition during the aqueous processing, nanocellulose-protected NMC electrodes exhibit higher initial coulombic efficiency (83% vs 62% at 0.1C) and capacity (133 vs 59 mAh g^{-1} at 6C) than unprotected electrodes. Additionally, optimized aqueous-processed NMC electrodes offer comparable or even superior electrochemical properties compared to the electrodes fabricated using the conventional toxic organic solvent, N-methyl-2-pyrrolidone. Consequently, the developed approach enables affordable, sustainable aqueous processing for Nickel-rich NMC 811 cathodes with excellent electrochemical performances.

1. Introduction

Lithium-ion batteries (LIBs) are being extensively investigated and developed to meet the growing demand for electric vehicles. Extensive research is currently being conducted on electrodes with high energy density and fast charging capabilities. The objective is to reduce the period of charging while simultaneously achieving a driving range that is equivalent to, or potentially exceeding, that of gasoline-powered automobiles. Although nickel-rich cathode materials such as $LiNi_{1-x-y}Co_xMn_yO_2$ (NMC) offer higher energy density compared to other commercial $LiFePO_4$ and $LiCoO_2$ cathodes, they lack stability in humid environments. This issue results in operational challenges and elevated manufacturing expenses associated with handling the hazardous and costly N-methyl-2-pyrrolidone (NMP) solvent.[1] Previous studies demonstrated that the poor humidity stability of NMC particles stems from the proton exchange process caused by the interaction between lithium ions (Li^+) and water molecules.[2] Upon proton exchange, migrated Li^+ reacts with atmospheric water and carbon dioxide to form LiOH, $LiHCO_3$, and Li_2CO_3,[3] which degrades the structure and the electrochemical performance of NMC.[4] Furthermore, the reaction products dramatically raise the pH of the slurry, corroding the aluminum (Al) current collector.[5]

Despite its challenges, water is an eco-friendly, cost-effective, and non-toxic solvent, underscoring the need to develop aqueous-processed NMC electrode manufacturing processes that achieve desirable electrochemical performance.[6] Beyond being applied to liquid-state LIBs, aqueous-processed electrodes possess the ability to overcome the constraints of conventional NMP-based

---

Y. Wang, L. Huang, J. Wang, H. Zhu
Department of Mechanical and Industrial Engineering
Northeastern University
Boston, MA 02115, USA
E-mail: h.zhu@neu.edu

The ORCID identification number(s) for the author(s) of this article can be found under https://doi.org/10.1002/adfm.202413865

DOI: 10.1002/adfm.202413865

Y. Fang, G. Wang
Department of Mechanical Engineering and Materials Science
University of Pittsburgh
Pittsburgh, PA 15260, USA
E-mail: guw8@pitt.edu

H. Zhou
X-Ray Science Division
Argonne National Laboratory
Lemont, IL 60439, USA

G. Wang, Q. Wu
Department of Chemical and Paper Engineering
Western Michigan University
Kalamazoo, MI 49008, USA

electrodes in solid-state batteries. The primary issue with NMP-based electrodes is the substantial interfacial resistance between the electrode and electrolyte.[7] NMP-based electrodes typically use fluorinated polyvinylidene fluoride (PVDF) as a binder, which is ionically insulating, highly crystalline, and lacks sufficient functional groups for modification.[8] In contrast, aqueous-based binders are reported to offer high ionic conductivity, enhanced adhesion, and greater modification potential.[9] These advantages reduce the interfacial resistance between the electrode and solid-state electrolyte, improving the electrochemical performances of solid-state batteries.[10] Consequently, exploring aqueous-based electrodes benefits both current LIBs and the advancement of solid-state battery technology. In summary, developing aqueous-processed NMC electrodes with promising electrochemical performance is challenging yet highly rewarding.

Currently, two main approaches are employed to enable aqueous-processed NMC electrodes: phosphoric acid introduction and current collector protection.[5,11] Previous studies demonstrated that adding phosphoric acid improves the electrochemical performance of aqueous NMC materials. The in situ generated protective phosphate layer limits further water penetration into the active material, while the residual acid buffers the pH value of the slurry to avoid corrosion of the current collector.[11a] Based on it, additional investigations about pH adjustment [12] and binder selection [13] further enhanced the rate performance and cycling stability of aqueous NMC electrodes. On the other hand, the Al current collector protection can be realized by the introduction of metal oxide that is employed to consume the produced alkaline substances and coating a carbon layer on the current collector to avoid direct contact between generated LiOH and Al foil.[11] However, the capacity of these aqueous-processed NMC electrodes is still inferior to that of NMP-based counterparts due to the significant consumption of lithium during the formation of the phosphate layer. Therefore, an ideal strategy involves the creation of a robust protective coating for NMC without sacrificing lithium or introducing new materials. Since the conductive additive cannot protect NMC,[14] the key of the matter arises if an aqueous-based binder can generate a functional coating layer on NMC particles during the electrode fabrication process.

Herein, we demonstrate for the first time the utilization of sustainable wood-derived nanocelluloses as a binder for moisture-sensitive nickel-rich cathode materials, specifically the single crystalline $LiNi_{0.8}Co_{0.1}Mn_{0.1}O_2$ (NMC 811), to confine water penetration and enable its aqueous processing. Considering that nanocelluloses are stable in LIBs[15] and their coating possesses exceptional water barrier properties to minimize the water infiltration into the enclosed substance,[16] the cellulose nanocrystal (CNC)-cellulose nanofiber (CNF) hybrid binder is applied to construct a dense, tough protective coverage for the NMC 811 particles in this work. Once the NMC particles and hybrid binder are mixed, a coverage automatically forms in aqueous environments on the NMC 811 surface, thus preventing proton exchange. Additionally, the first principles of density functional theory (DFT) calculations predict that the functional group of CNF exhibits stronger binding strength with NMC particle surface than water molecules, and the tendency of Li^+ moves to the NMC surface could be suppressed by the CNC and CNF coating. These results suggest that the rapid formation of protective cellulose coating covering NMC particles is possible, leading to a reduction in proton exchange during water processing. Furthermore, for the first time, the analysis of wide-angle X-ray scattering (WAXS) accurately measures the dimension of nanochannels within CNF and CNC, combines molecular dynamics (MD) simulation to understand the cellulose-water interactions, as well as proposes that the hydrophilic celluloses could effectively trap interlayer water into their nanochannels and thus prevent water from penetrating the NMC particles. After being protected by CNC-CNF coating, the NMC 811 electrodes display dramatically improved capacity at various charge rates as compared to conventional aqueous-based electrodes. More impressively, the fabricated aqueous-based CNC-CNF electrodes exhibit comparable or even superior electrochemical performances compared to commercialized NMC 811 electrodes fabricated using toxic NMP solvent and PVDF binder. Consequently, the developed aqueous electrode slurry is suitable for economical and environmentally friendly operational roll-to-roll manufacturing.

2. Results and Discussion

Under aqueous conditions, NMC materials decompose due to outward Li^+ migration and inward hydrogen ion (H^+) migration. As **Figure 1A** shows, the proton exchange triggers chemical reactions that consume lithium, creating LiOH and Li_2CO_3 deposits. The LiOH formation reduces capacity of NMC, increases the pH value of slurry, and consequently erodes the Al current collector. Introducing nanocelluloses is attempted to suppress these reactions by rapidly creating a protective layer, as illustrated in Figure 1B. Due to carrying a negative surface charge in water, nanocelluloses are attracted to NMC particles with a positive charge through electrostatic force. Moreover, the abundant hydroxyl (—OH) groups of cellulose, highly acidic sulfonate (—HSO_3) groups on CNC, and carboxyl (—COOH) groups of CNF have superior adsorption kinetics to the NMC than water molecules. Therefore, CNC and CNF can be preemptively adsorbed on the surface of NMC particles to form a uniform, dense, and tough protective layer. It makes NMC isolated from water, thus avoiding the generation of precipitation. As illustrated in Figure 1C, the unique nanochannels of cellulose inter-chain increase the water penetration tortuosity and trap the interlayer water. This dense networking forms the functional nanocellulose barrier coating that serves to delay or prohibit the ongoing proton exchange between NMC and water, resulting in the successful development of aqueous-based NMC electrodes with high energy density.

CNC and CNF are nanomaterials derived from bulk cellulose extracted in large quantities from abundant tree resources (**Figure 2A**). Cellulose and water are the major components of trees, and their interactions are crucial for both fundamental research and practical applications of nanocelluloses. Specifically, in this work, a deep investigation of the cellulose-water interactions reveals the underlying mechanism that the cellulose prevents water molecules from penetrating and proton exchange. Although cellulose-water interactions are essential, the related accurate structural characterization at the angstrom level is highly challenging.[17] Considering the interfacial spacing between two cellulose chains is a sub-nanometer scale, WAXS is one of the few feasible approaches to assess the dimension of

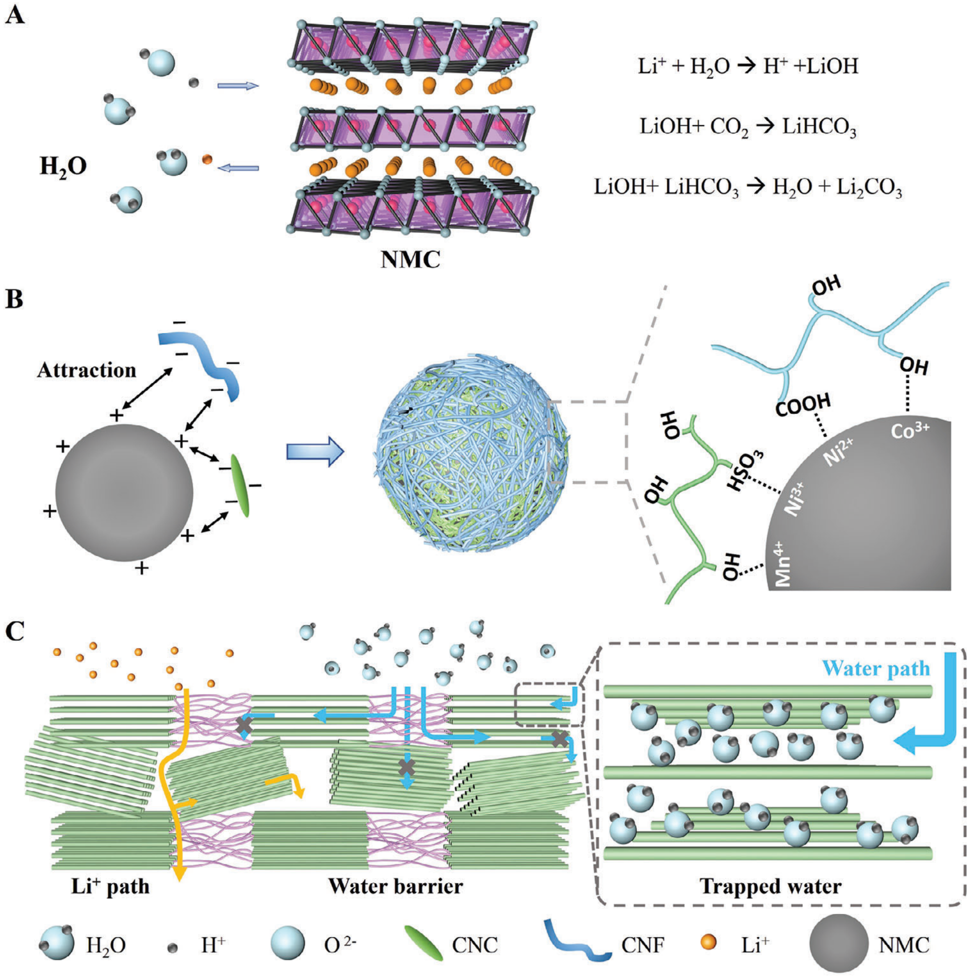

Figure 1. Schematics of nanocellulose enabling aqueous-processed NMC particles. A) Proton exchange reaction between NMC particles and water molecules. B) Mechanisms of the nanocelluloses coverage formation. C) CNC-CNF coverage blocks free water penetration by capturing interlayer water during manufacturing and allows Li-ion transfer during cycling.

nanochannels and cellulose-water interactions.[18] The structure of the nanochannels of CNC and CNF varies owning to their different chemical groups and dimensions resulting from their different fabrication processes (Figure 2B). Specifically, CNC was synthesized via sulfuric acid hydrolysis, during which the disordered amorphous components were removed, and certain —OH groups were sulfonated with —HSO$_3$ groups. This technique hardly alters the dimensions of the nanochannels.[19] CNF was prepared by 2,2,6,6-tetramethylpiperidine-1-oxyl (TEMPO) oxidation, leading to the replacement of a portion of —OH at C6 on glucose with —COOH groups. During TEMPO oxidation, substantial amounts of carboxylate and aldehyde groups are introduced, leading to an increase in electrostatic repulsion between these charged celluloses, which in turn enlarges the inter-chain spacing of nanofibers.[20] The oxidation of CNF is determined by various experimental parameters, and the celluloses are incompletely oxidized, leaving some cellulose with the original spacing. In addition, the majority of the amorphous regions of cellulose persist to create long and flexible fibers.[21]

WAXS is a powerful tool to study the crystal structure of polymers at the atomic level. Thus, WAXS at an X-ray energy of 13.5 keV with a wavelength of 0.91837 Å was employed to characterize the structure of CNC and CNF under wet and dry circumstances. The distance between two cellulose chains is calculated according to Bragg's law (Equation 1).

$$n\lambda = 2d\sin\theta \tag{1}$$

here, λ is the X-ray wavelength, θ is the angle of incidence, and d represents the distance between the atomic layers in the lattice. n is the integer number for the order of the diffraction. As shown in Figure 2C,D, both CNC and CNF exhibit representative peaks of (110), (200), and (004) at 2θ values of about 9.50°, 13.80°, and 10.40°. In comparison to dry nanocelluloses, an additional peak was detected at 6.01° for wet nanocelluloses, indicating an interatomic spacing of 8.77 Å, and corresponding to a monolayer of water molecules that is absorbed on both sides of a cellulose chain (Figure 2E). The monolayer of interlayer water has a thickness of 2.80 Å[22] and the computationally calculated cellulose chain has a thickness of ≈5.00 Å (Figure S1, Supporting Information). Compared to CNC, a notable peak at 4.76° is found in both wet and dry CNF samples, demonstrating an interatomic

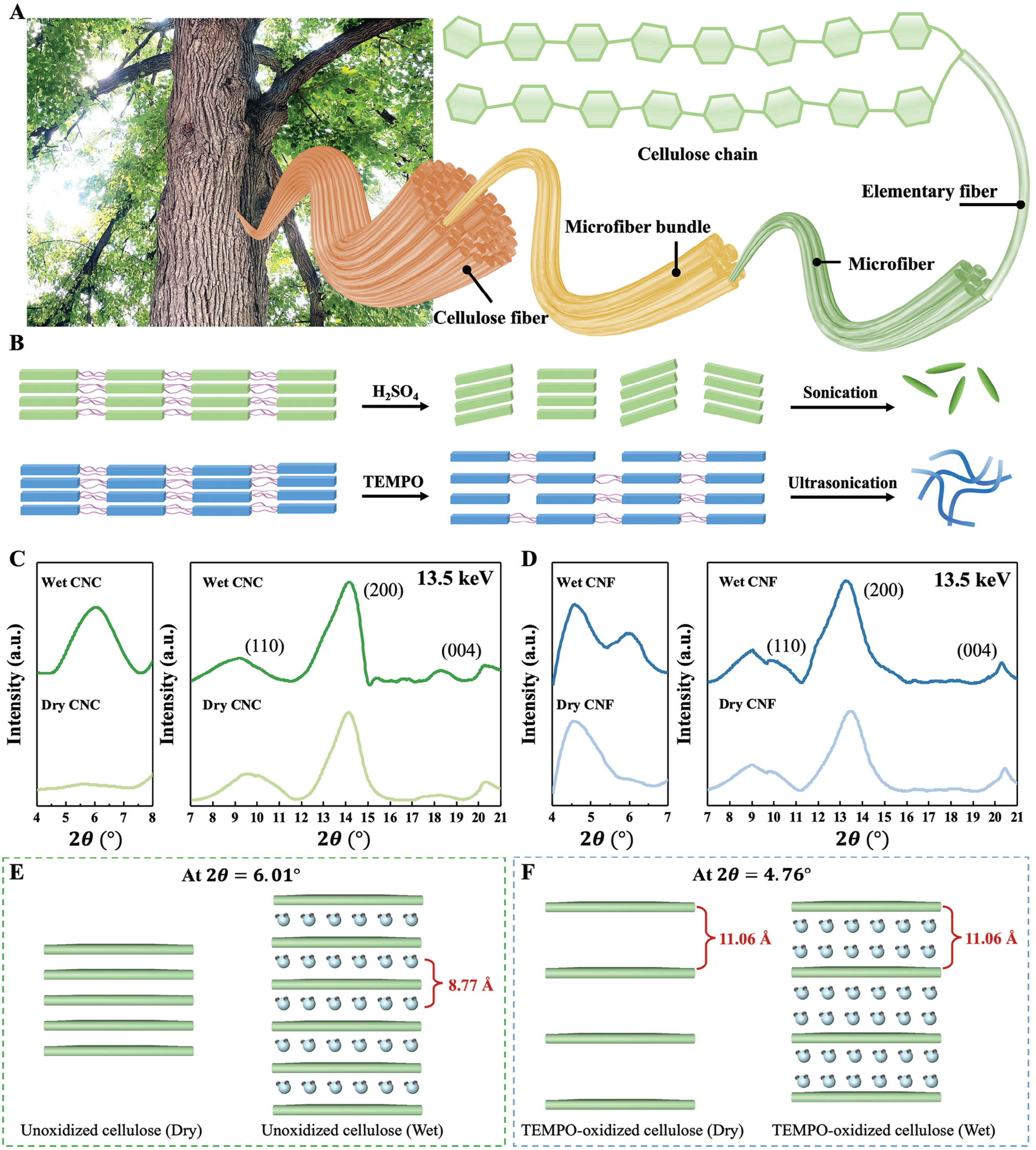

Figure 2. Interactions between nanocellulose and water. A) The CNC and CNF are derived from trees. B) The structure of CNC and CNF is affected by their preparation methods. C) WAXS patterns of wet and dry CNC. D) WAXS patterns of wet and dry CNF. Schematics of cellulose channels and water molecules captured in E) unoxidized and F) TEMPO-oxidized celluloses.

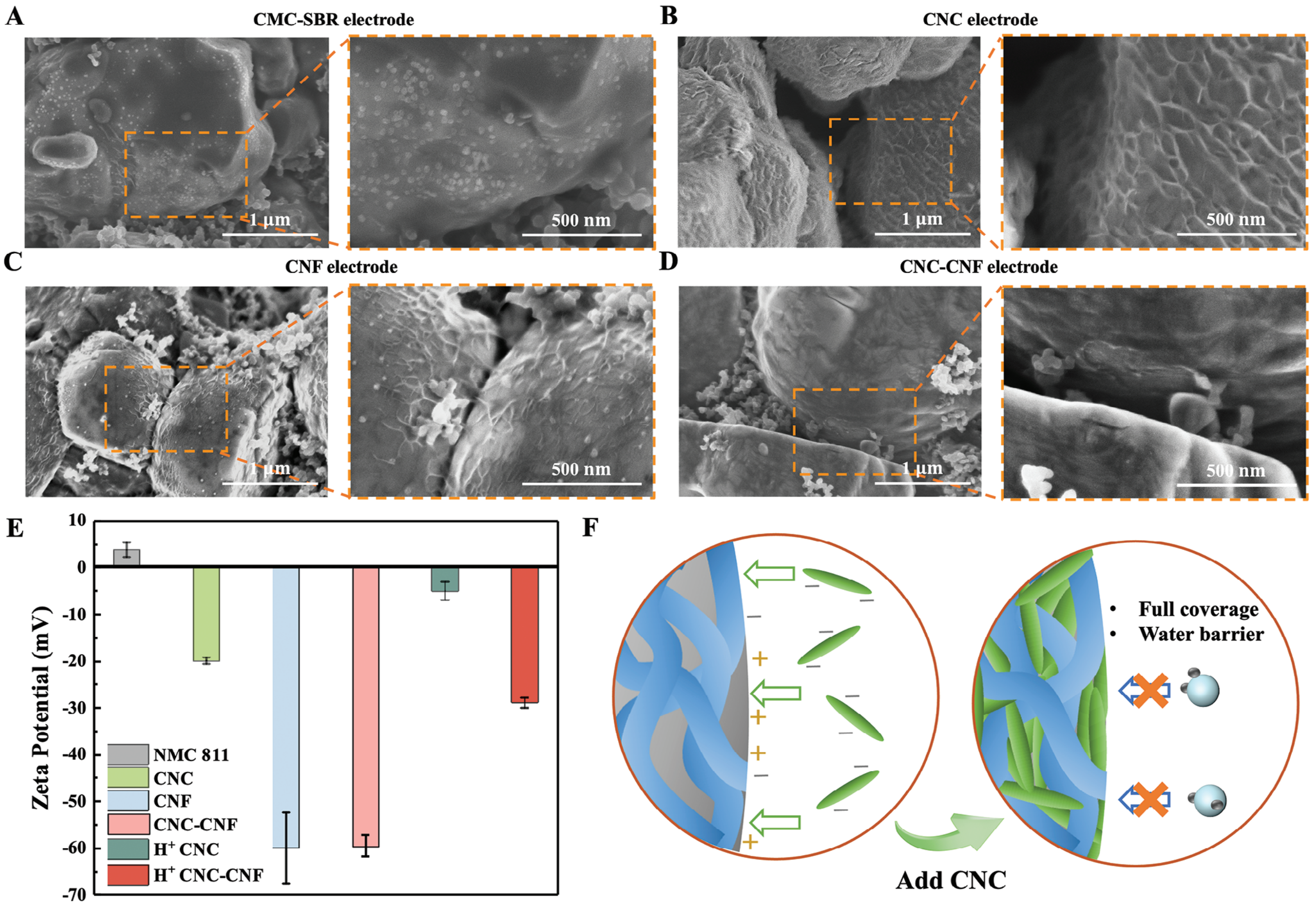

Figure 3. Characterizations and mechanism of nanocellulose coating on NMC 811 particles. SEM images of NMC 811 coated with A) CMC-SBR binder, B) CNC binder, C) CNF binder, and D) CNC-CNF binder. E) Zeta potential of NMC 811 particles and nanocelluloses in aqueous. F) Schematic of dense CNC-CNF coverage formation.

spacing of 11.06 Å. This spacing corresponds to the partially TEMPO-oxidized and swelled nanochannels of the inter-chain within CNF. As depicted in Figure 2F, the structure of these swelled nanochannels is very stable and is not influenced by water molecule insertion. The spacing of 11.06 Å indicates the fact that nanochannels of CNF can hold up to around two layers of water molecules. Simulations reveal that these interatomic spacings efficiently trap and confine water molecules, preventing their penetration into NMC particles. Further in-depth understanding through simulations will be provided later.

Scanning electron microscopy (SEM) was applied to visually elucidate the morphology of nanocellulose protection layers and related NMC particles. Compared to the smooth surface of pristine single crystalline NMC 811 particles (Figure S2, Supporting Information), the conventional aqueous electrode with carboxymethylcellulose and styrene-butadiene rubber (CMC-SBR) binder exhibited numerous inhomogeneous white dots on the NMC particles (**Figure** 3A). The white dots are likely LiOH and Li_2CO_3 deposits formed by unimpeded reactions between water molecules and NMC particles.[2] In contrast, the CNC (Figure 3B) and CNF (Figure 3C) electrodes displayed fluffy, wrinkled coatings tightly wrapping the NMC particles. Comparatively, the CNC-CNF hybrid binder imparted complete NMC particle coverage. This dense and smooth coating makes it difficult to distinguish from the NMC itself. Figure 3D shows a minor defect in the CNC-CNF coating, highlighted and colored in Figure S3 (Supporting Information). Fluorescently stained nanocellulose and NMC mixture exhibit intense fluorescence in the form of spheres (Figures S4 and S5, Supporting Information), demonstrating the existence of the CNC-CNF coverage on the NMC particle surfaces. More analysis is discussed in the Supporting Information. In summary, proper functional CNC-CNF nanocellulose coatings are successfully constructed on the NMC surfaces. The ideal coating is beneficial for reducing the accession of water molecules and minimizes the NMC particle decomposition. The soluble base content test was applied to evaluate the amounts of LiOH and Li_2CO_3 side products for the aqueous-based NMC electrodes. As listed in Table S1 (Supporting Information), the CNC-CNF binder delivers about one-fourth of the deposit concentration of CNC-CNF electrodes (1.74 wt.%) than CMC-SBR

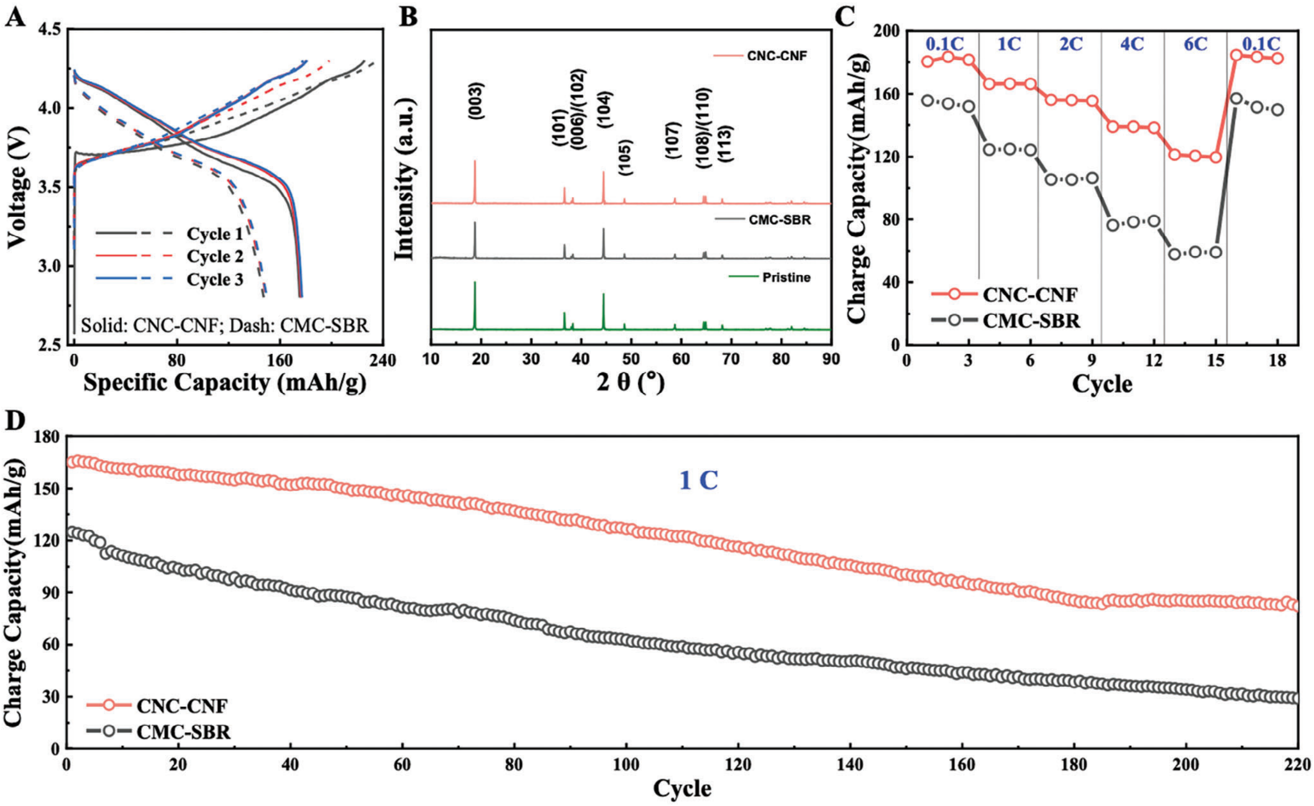

Figure 4. Comparative analysis of aqueous binders: CNC-CNF versus CMC-SBR. A) Galvanostatic charge–discharge curves of CNC-CNF (solid line) and CMC-SBR (dash line) electrodes at the current rate of 0.1C. B) XRD, C) rate performance and D) cycling stability of aqueous-processed NMC 811 electrodes with CNC-CNF and CMC-SBR as binder individually.

electrodes (4.82 wt.%), demonstrating the outstanding protection ability of the CNC-CNF binder for NMC 811 particles in the aqueous condition.

To investigate the formation of the dense CNC-CNF protective layer and understand the interaction between NMC particles and nanocellulose in water, the surface charge of the materials was assessed. Figure 3E presents the zeta potentials of uniform binder suspensions (Figure S6, Supporting Information). NMC 811 surfaces presented a positive zeta potential value of +3.8 mV. In contrast, the nanocelluloses displayed negative values. Specifically, zeta potentials of CNC, CNF, and CNC-CNF are −20, −60, and −59 mV at the ambient temperature, respectively. More negative values indicate higher surface negative charge concentrations. Additionally, fresh hydrolyzed CNC contains some acid before dialysis, leading to less negative zeta potential values of H^+ CNC (−5 mV) and H^+ CNC-CNF (−29 mV). Owing to electrostatic attraction, nanocelluloses automatically migrate to positively charged NMC 811 in water, forming a dense and thin protective coating.

Moreover, the movement kinetics of these celluloses depend on their surface charge. Figure 3F shows the formation mechanism of the CNC-CNF hybrid nanocellulose coating. When NMC 811 is introduced to the nanocellulose suspension, electrostatic interaction derives CNF and CNC move toward NMC particles. Remarkably, soft CNF with a high aspect ratio and high negative charge concentrations enables it to envelop the NMC surface as a loose cobweb. Subsequently, rod-shaped CNC completes this coating layer by adhering as patches to areas on the NMC surface not fully covered by CNF since the opposite charges between CNC and NMC particles. This collaborative action results in a more complete encapsulation of the entire NMC particle than CNF or CNC alone (Figure S7, Supporting Information), thus effectively isolating the NMC particle from water.

In order to assess the beneficial effects of nanocellulose coatings on aqueous-processed NMC electrodes, the electrochemical performance of CNC-CNF and CMC-SBR electrodes was evaluated. **Figure** 4A shows the initial three galvanostatic charge–discharge curves of CNC-CNF and CMC-SBR electrodes at 0.1C ($1C = 200 \text{ mAh g}^{-1}$). The absence of abnormal plateaus indicates no side reactions and good electrochemical stability of these aqueous-based binders during cycling. The initial charge and discharge capacities of the CNC-CNF electrode were 225 and 175 mAh g^{-1}, respectively, with an initial coulombic efficiency of 78%. In contrast, the charge and discharge capacities of the CMC-SBR electrode were 236 and 147 mAh g^{-1}, delivering a pretty low initial coulombic efficiency of 62%. The efficiency was influenced by the creation and stability of the cathode electrolyte interface (CEI), demonstrating the complete CNC-CNF coverage reduced adverse side products, providing a stable CEI during charging and discharging. The following two cycles of CNC-CNF electrodes show similar capacities, indicating the commendable stability of aqueous-based CNC-CNF electrodes.

Unlike that, more energy is needed to construct the stable CEI for the CMC-SBR electrode. Concurrently, the CNC-CNF electrode rendered a much higher discharge capacity than the CMC-SBR electrode, further demonstrating the protective effects of the CNC-CNF coating in water.

In order to evaluate the effects of CNC-CNF and CMC-SBR binders for NMC particle protection, X-ray diffraction (XRD) analysis of NMC 811 before and after mixing with these binders is presented in Figure 4B. All samples exhibited clear split of (108) and (110) peaks about $2\theta = 65°$, indicating the bulk structure and layered structure of NMC particles are well maintained since the reaction occurred on the surface. However, the integrated intensity ratio of (003) and (104), I(003)/I(104), are various. The I(003)/I(104) values represent the degree of cation mixing. The higher the value, the lower the cation mixing, resulting in superior electrochemical performances.[23] In this work, the I(003)/I(104) value of pristine NMC 811 particles (1.497) is close to that of CNC-CNF composited particles (1.458) and significantly higher than that of the NMC particles covered by CMC-SBR (1.199). As a result, conventional water processing exacerbates the cation mixing of the CMC-SBR electrode and responds to poorer capacity than the CNC-CNF electrode.

Figure 4C displays the rate performance of these two electrodes charged from 0.1 to 6C. Since fewer NMC particles structural decay, the CNC-CNF electrode performs an acceptable charge capacity of 182, 166, 156, 139, and 120 mAh g^{-1} at current densities of 0.1, 1, 2, 4, and 6C. As the comparison sample, the CMC-SBR electrode imparts much lower average charge capacities of 154, 124, 105, 78, and 59 mAh g^{-1} at the related charge current rates. It is worth noting that the CNC-CNF electrode demonstrates a twofold increase in charge capacity than the CMC-SBR electrode at 6C. In addition, as shown in Figure 4D, the CNC-CNF electrode maintains a higher charge capacity than the CMC-SBR electrode throughout the 200 cycles. At the 200th cycle, the CNC-CNF electrode demonstrates nearly twice the capacity retention than the electrode using the traditional aqueous-based binder. Due to the different coating effects of CNC and CNF with various ratios on NMC particles, the final electrochemical properties are different (Figure S8, Supporting Information).

Generally, CNC is hydrolyzed using high concentrations of sulfuric acid, which are subsequently eliminated via dialysis to yield the final product.[24] In this study, retaining the residual acid benefits the electrochemical properties of aqueous NMC electrodes. As shown in **Figure** 5A, the acid lowers the pH value of the electrode slurry, avoiding the Al current collector corrosion. Al is chemically resistant to corrosion in the pH range of 4–9, which is stable with electrode slurry using H^+ CNC-CNF as a binder (pH of 8.37) but not stable with electrode slurry using CNC-CNF binder (pH of 10.25) and electrode slurry using CMC-SBR binder (pH of 11.23). SEM images of current collectors with the electrode materials removed (Figure 5B; Figure S9, Supporting Information) reveal some corrosion traces for CMC-SBR but none for H^+ CNC-CNF. Preventing corrosion avoids decreasing the electronic conductivity of the current collector (Figure S10, Supporting Information) and ensures electrode-collector contact. Meanwhile, skipping the dialysis step reduces both the duration and expenses, rendering it appropriate for the industrialization of aqueous-processed NMC electrodes.

Further electrochemical performance investigations about CNC-CNF aqueous electrodes with and without acid were characterized. Figure 5C compares the initial three charge–discharge curves of CNC-CNF and H^+ CNC-CNF electrodes at 0.1C. No additional plateaus were observed, indicating that the acid did not cause any unexpected reaction. Moreover, the acid-included electrode provides a higher initial discharge capacity (181 vs 175 mAh g^{-1}) and superior initial coulombic efficiency (83% vs 78%) than the CNC-CNF electrodes because of the formation of a more stable CEI. Both electrodes show similar capacities in the subsequent two cycles, suggesting reasonable stability. Figure 5D depicts Nyquist plots of CNC-CNF and H^+ CNC-CNF electrodes. The charge transfer resistances of CNC-CNF electrodes with and without acid are 318 and 470 Ω, respectively. This charge transfer resistance results in enhanced rate performances of the H^+ CNC-CNF electrodes, as shown in Figure 5E. At a low current rate of 0.1C, the capacity of two electrodes is 182 mAh g^{-1} without a distinguishable difference, while the H^+ CNC-CNF electrode shows higher capacity than the CNC-CNF electrode from 1C, and this difference is enlarged with current rates increasing. Furthermore, compared to published aqueous binders, the H^+ CNC-CNF binder provides a remarkable capacity for aqueous-processed NMC electrodes (Figure S11, Supporting Information).

The current collector erosion not only impedes the electron transfer between the electrode and the current collector resulting in reduced capacity of the CNC-CNF electrode at high rates but also negatively impacts the cycling stability of electrodes. As displayed in Figure 5F, the H^+ CNC-CNF electrode shows a capacity of 137 mAh g^{-1} with a capacity retention of 80% at the 300th cycle and a capacity retention of 70% at the 550th cycle under the current rate of 1C, which is much stabler than the CNC-CNF electrode. During cycling, the CNC-CNF electrode exhibits a slow decrease in capacity, and its charge capacity suddenly drops at the 223rd cycle. The improved cycling stability of the H^+ CNC-CNF electrode due to the Al is erosion-free, which ensures a good bonding between the electrode and the current collector. Since both acid and the formulation of hybrid nanocellulose play important roles in this aqueous-processed NMC electrodes, more comprehensive screening has been studied to achieve the best electrochemical performance of H^+ CNC-CNF electrodes (Figures S12 and S13, Supporting Information). From the result, we concluded the CNC:CNF = 1:2 has the best performance.

Based on an assessment of the economic, environmental, and operational advantages, it is desired that aqueous-processed NMC electrodes can render electrochemical performances that are equal to, or possibly superior to, those of commercial NMC electrodes manufactured using the toxic and expensive NMP solvent. If superior electrochemical properties can be achieved, it is anticipated to facilitate the widespread adoption and commercialization of aqueous-processed NMC electrodes in industry. Consequently, the electrochemical performances of the aqueous-processed NMC electrode utilizing an optimized nanocellulose binder were evaluated in comparison to the NMP-processed NMC electrode employing the PVDF binder. The PVDF electrode shows significantly larger charge transfer resistance than the H^+ CNC-CNF electrode, contributing to a lower charge capacity at high rates over 1C (Figure S14, Supporting

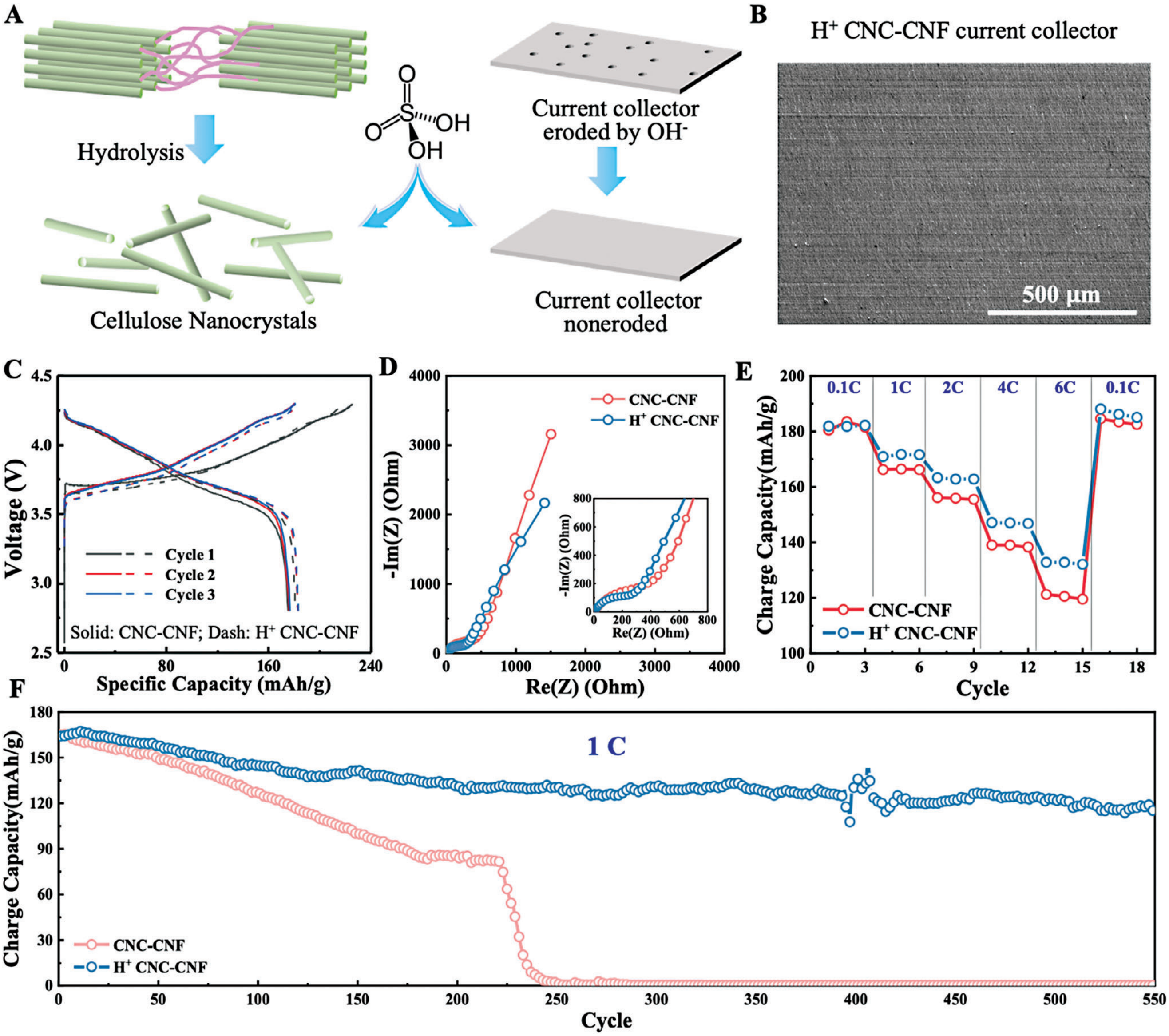

Figure 5. Electrochemical performance of NMC 811 electrode using CNC-CNF binders with and without acid. A) Schematics of the role sulfuric acid plays in CNC synthesizing procedure and protect current collector of NMC electrode. B) SEM images of the current collector with H^+ CNC-CNF as binder after removing electrode materials. C) Galvanostatic charge–discharge curves, D) Nyquist plots, E) rate performance, and F) cycling stability of the aqueous-based H^+ CNC-CNF and CNC-CNF electrodes.

Information). The main reason for the lower charge transfer resistance is that cellulose wetted with electrolytes has higher lithium ion conductivity compared to PVDF.[25] More impressively, the optimized aqueous-based H^+ CNC-CNF electrode delivers much superior cycling stability than the NMP-based PVDF electrode using Li metal as an anode (Figure S15, Supporting Information). Considering the fact that it is not entirely consistent with the focus of this manuscript, related results are shown in Figures S16–S18 (Supporting Information) and discussed in the Supporting Information. Furthermore, this aqueous-based H^+ CNC-CNF NMC slurry can be easily used to fabricate structural tailorable electrodes for fast-charging electrode manufacturing (Figures S19 and S20, Supporting Information).

To understand the protective effects of CNC and CNF coating on NMC particles, the DFT calculations were performed to predict the adsorption energies of the H_2O molecule, —R—COO (the functional group of CNF, R represents $C_5H_7O_4$ and is simplified as CH_3 to reduce calculation cost), and $-HSO_3$ (the functional group of CNC) on the surface of NMC electrode and the surface segregation energy of Li in the NMC electrodes covered by these surface adsorbates. Here, the adsorption energies were calculated by subtracting the energies of the isolated components from the energy of the adsorbed system (**Figure** 6A). More negative adsorption energy indicates stronger binding of the adsorbate to the NMC surface.[26] The computational results (Table S2, Supporting Information) show that the adsorption energies of —R—COO

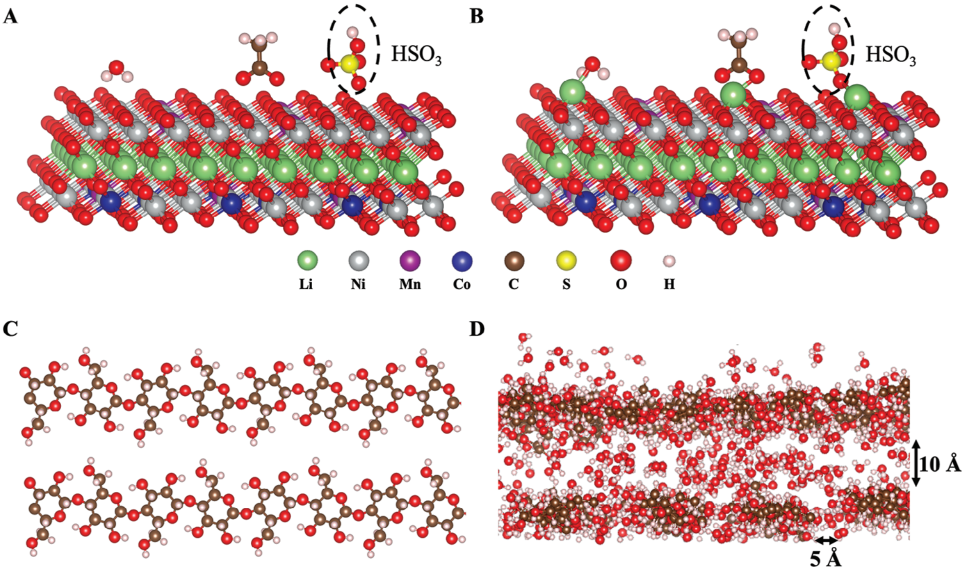

Figure 6. Simulation results. A) Atomic structure of H_2O, CH_3COO, HSO_3 groups adsorbed on NMC surface. B) Delithiated NMC electrode with Li^+ moving from the subsurface to the surface 3b sites of NMC surface under H_2O, —R—COO, —HSO_3 adsorption. C) Atomic structure of two parallel cellulose chains. D) Snapshot of two layers of cellulose interacting with water obtained from an NVT MD simulation at 600K.

are lower than those of H_2O, indicating a relatively higher tendency for the CNF functional group to cover the NMC surface than water. This result explains why CNF and CNC can tightly wrap the NMC particles and form the coating (Figure 3). Moreover, the Li surface segregation energy was calculated as the energy difference between the configurations with Li in the bulk region and the surface of the NMC electrode (Figure 6B). The negative value of Li surface segregation energy indicates a higher tendency for the adsorbate to attract Li ions to the surface.[2] Our results show that the NMC electrode covered by H_2O would have negative Li surface segregation (i.e., −0.89 eV), whereas the NMC covered by —R—COO and —HSO_3 groups have positive Li surface segregation energies. This result suggests that the presence of polymer coatings containing —R—COO and —HSO_3 groups could impede the Li ions migration toward the NMC surface, thus offering protection against Li^+ depletion and degradation. Notably, the NMC covered by —R—COO was predicted to have even higher positive Li surface segregation energy, as shown in Table S3 (Supporting Information), than that of the NMC covered by HSO_3, implying that polymer CNF with —R—COO groups would exhibit better performance in preventing Li segregation to the surface than polymer CNC. This computational prediction is consistent with the experimental observation (Figure 4C) that CNF (with —R—COO groups) coated electrode has higher discharge capacity than CNC (with —HSO_3 groups) coated electrode. In summary, our DFT results predict that functional groups —R—COO and —HSO_3 of the polymer coating tend to cover the NMC surface and further effectively impede the loss of Li from the NMC electrode in an aqueous environment.

Furthermore, the Molecular Dynamics (MD) simulations were carried out to gain insights into the interaction between liquid water and the main chain of CNC and CNF polymer coating. The porous structure of the main chain of CNC and CNF coating was the same and modeled by repeatedly packing the cellulose polymer chains (shown in Figure 6C) in parallel in one layer and rotating the chains by 90° in the subsequent layer, as shown in Figure S21 (Supporting Information). The separation of the polymer chains was set to be 5 Å within each layer, whereas the interlayer spacing was varied to be 5, 10, and 15 Å, respectively. The H_2O molecules with a density close to that of liquid water (i.e., 1 g cm^{-3}) were added into the space between the cellulose chains. Figure 6D shows an equilibrated structure of the system after 100 ps of MD simulation, and the trajectory animation is shown in Video S1 (Supporting Information). The MD simulations show that a small amount of H_2O could diffuse out of the polymer coating while most of the H_2O could be retained inside the polymer coating. Quantitatively, the MD simulations predicted that the cellulose coating with an interlayer spacing of 10 Å keeps the highest ratio of water inside (94%) as compared to 91% with 15 Å interlayer spacing and 72% with 5 Å interlayer spacing. The same trend has also been observed from the MD simulations for the cellulose coating with a chain separation of 15 Å within each layer. It should be mentioned that the analysis of WAXS patterns shows the spacing in CNF is larger than that in CNC. Consequently, our MD simulation results suggest that an increase in the interlayer spacing in the TEMPO-oxidized CNF could be beneficial in retaining water within the coating and protecting NMC from water-induced damage during aqueous processing. Thus, the MD simulation results explain the observed improvement in initial discharge capacity and initial Coulombic efficiency of the CNF-coated electrode compared to the CNC-coated electrode.

3. Conclusion

This study facilely fabricated aqueous-processed NMC 811 electrodes that exhibit comparable electrochemical performances of the conventional electrodes fabricated using the toxic and costly NMP solvent. Sustainable, biodegradable, and functionable nanocelluloses were applied as a aqueous binder to form a dense protective coating over NMC particles. For the first time, WAXS is applied to precisely measure the interatomic spacing of the nanochannel in the nanocelluloses, and it is demonstrated that these nanochannels have the capability to confine the interlayer water molecule's movement through simulation. This dense nanocellulose protective layer exhibits the potential to impede the penetration of water molecules, hinder proton exchange, prevent lithium loss, limit cation mixing of NMC particles, and inhibit NMC structural decomposition in aqueous. Compared to utilizing commercial water-based CMC-SBR binder, the CNC-CNF binder imparts an aqueous-processed NMC electrode with improved initial coulombic efficiency (78% vs 62%) at the low rate of 0.1C, enhanced capacities at all current rates, as well as superior cycling stability (about twice the capacity retention at 1C at the 200th cycles). More interestingly, leftover sulfuric acid from CNC hydrolysis processing proves valuable for ensuring Al current collector integrity and enhancing aqueous NMC electrode cycling stability. After optimization, the H^+ CNC-CNF electrode achieved an outstanding charge capacity of 133 mAh g^{-1} at 6C, surpassing the performance of the CMC-SBR electrode (59 mAh g^{-1}) and CNC-CNF electrode (120 mAh g^{-1}). Concurrently, the H^+ CNC-CNF electrode delivers 70% capacity retention at the 550th cycle under the current rate of 1C, while the CNC-CNF electrode suffers a significant capacity drop from the 223rd cycle. The improved stability is attributed to the fact that the H^+ CNC-CNF slurry does not corrode Al foil, maintaining good contact between the electrode and the current collector. Furthermore, this aqueous-based H^+ CNC-CNF electrode demonstrates enhanced rate performance and cycling stability than NMP-based PVDF electrodes using Li metal as the anode. This aqueous-based NMC slurry can be utilized in industrialization and substitutes current NMP-based slurry while fulfilling the demands for high electrochemical capacity, economic feasibility, manufacturing convenience, and environmental sustainability. Therefore, this aqueous-processed NMC electrode holds the potential to considerably broaden the market prospects of NMC LIBs in the future.

4. Experimental Section

Materials: Microcrystalline cellulose, 98% sulfuric acid, 2,2,6,6-tetramethylpiperidine-1-oxyl (TEMPO), Sodium bromide (NaBr), Sodium hypochlorite solution (NaClO solution), fluorescein sodium salt (NaFl, $C_{20}H_{10}Na_2O_5$), and Polyvinylidene fluoride (PVDF) were procured from Sigma–Aldrich, USA. Carboxymethyl cellulose sodium salt (CMC) and hydrochloric acid (HCl) were purchased from Thermo Scientific, USA. Single crystalline NMC 811 was purchased from Easpring Material Technology Co., LTD., China. Super P, Styrene-butadiene rubber (SBR) solvent (50 wt.% in water), and Al foil current collector were procured from MTI Co., USA. NMP was procured from Fisher Science Education, USA. Before ink preparation, NMC 811 and Super P powders were dried in a vacuum oven (MTI Co., USA) for at least 12 h at 100 °C.

Cellulose Nanocrystal Synthesis: The CNC acid hydrolysis process was based on the previous work.[27] In brief, 30 g of microcrystalline cellulose was mixed with 300 mL of 64 wt.% sulfuric acid under constant mechanical stirring for 40 min at 45 °C. Ten times the volume of water was applied to terminate the reaction. The suspensions were washed with deionized (DI) water using centrifuging (Thermo Scientific, USA) at 4000 rpm. Once the supernatant became turbid, the centrifuge step was done. The pH of the collected supernatant was 1.33 measured by an Oakton PC 450 pH meter. To remove the remaining acid, the resulting suspensions were dialyzed with DI water using dialysis membranes (molecular weight cutoff of 12,000–14000) until the pH of the water was ≈7.

Cellulose Nanofiber Synthesis: CNF was prepared by TEMPO-mediated oxidation following mechanical disintegration.[28] In brief, softwood pulp (20 g with ≈85% water content) was dispersed using mechanical stirring for 2 h. And then, TEMPO (0.02 g g^{-1}) and NaBr (0.15 g g^{-1}) solutions were mixed, and 10 mmol g^{-1} of 12.5% NaClO solution was added dropwise. Following that, 0.5 mol L^{-1} NaOH solution was applied to adjust and keep the pH to 10.5 overnight. The oxidation reaction was terminated by 5 mL of ethanol. The synthesized CNF was washed and filtrated using DI water. The final suspension was well-dispersed in an ice bath with a Prob sonicator (Sonics & Materials, Inc.)

Electrodes Preparation: The binders were dispersed or dissolved into the corresponding solvents to achieve the concentration of 3 wt.% before use. The pristine NMC 811, Super P, and binder were added with a weight ratio of 92:5:3. Specifically, the pristine NMC 811 was mixed with Super P for 5 min in a dual asymmetric centrifugal mixer (DAC 330-100 Pro Speedmixer from FlakTek), then the prepared hybrid binder was added to the powder mixture and mixing for 5 min by the mixer. No extra treatment was required for the NMC 811 particles. In the absence of special instructions, the ratio of the masses of CNC to CNF in the CNC-CNF hybrid binder was 1:1 and the ratio of the masses of H^+ CNC and CNF in the H^+ CNC-CNF hybrid binder was 2:1. The ratios were screened through the electrochemical performances, as shown in Figures S8 and S13 (Supporting Information). After all, components were evenly mixed, the pH value of acid-included H^+ CNC:CNF = 4:1, H^+ CNC:CNF = 2:1, H^+ CNC:CNF = 1:1, H^+ CNC:CNF = 1:2, and H^+ CNC:CNF = 1:4 electrode slurries were 7.44, 7.79, 8.37, 9.26, and 9.79, respectively. All electrode slurries exhibit slightly alkaline, and this residual alkaline did not cause negatively affected side redox reactions in related electrodes. Then, slurries were coated on Al foil using the doctor blade method. Electrodes were dried in a desiccator and transferred into a vacuum oven (from MTI Co., USA) for at least 4 h at 100 °C before being transferred to the glove box.

Characterization Methods: The X-ray diffraction (X'Pert Pro, Philips) with Cu Kα radiation was used to characterize the structure and orientation of CNC and NMC particles that were pretreated with various binders. Before measuring the mixture, the NMC and binders were mixed with a weight ratio of 92:3, which consists of that in electrodes. The wide-angle X-ray scattering (NSLS-II 11-BM) of CNC and CNF was measured with X-ray energy of 13.5 keV, sample-to-detector distance of 253 mm, and wavelength of 0.91837 Å. The morphology of the samples was observed using a Hitachi S4800 scanning electron microscopy set at 3 kV. Nano ZS Zetasizer (Malvern) was applied to measure the zeta potential of NMC particles and nanocelluloses in water.

Electrochemistry Characterization: The electrolyte used in all electrochemical tests was 1.2 м LiPF6 dissolved in EC:EMC = 3:7 by weight (Gen 2). During the assembly, 80 µL of electrolyte was added to the cell assembly. The separator was Celgard 2400 (25 µm in thickness). The 110 µm Li metal was applied as the anode. The active materials mass loading of the electrode was ≈4.5 mg cm^{-2}, with a thickness of 35 µm. EIS was done at room temperature using an electrochemical station (Biologic SP150) in the frequency range of 1 MHz–100 mHz and fitted by ZView software. A LANDT 8-channel tester (Wuhan LAND Electronic Co., Ltd.) was used for galvanostatic testing. Considering practical and broader commercial and industrial fast-charging electrode applications in the future, the rate performance was measured using a special setting for a fast-charging cathode. Specifically, all cells charged at various C-rates, 0.1C for six cycles, then 1C, 2C, 4C, and 6C for three cycles, and finally recovered to 0.1C for another three cycles. After charging, all cells discharged at a consistent current rate of C/3. The cycling stability test was charged at 1C and discharged at C/3. All cells were initially activated at 0.1C for six cycles. All electrochemical measurements were performed at room temperature of 25 °C.

Fluorescence Analysis: The 3% solid content nanocellulose binder was mixed with a 0.25 mg mL^{-1} fluorescent water solution with a weight ratio of 2000:9. The mixture was stirred for 48 h away from light. Then, the suspension was washed by filtering several times until the filtered water was transparent. The suspension and the filtered water were mixed with the NMC particles. The weight ratio of NMC:binder = 92:3. After drying, the mixture was observed by optical microscopes (Zeiss Axio Observer and Zeiss LSM 880).

The Soluble Base Content Test: The soluble base content test followed the previous work.[29] Briefly, 100 g of de-ionized (DI) water was mixed with 1 g electrode powder in a flask for 10 min. Subsequently, the slurry was promptly subjected to filtration. 90 g of the filtrated solution was employed for the pH titration experiment in a 250 ml glass flask. Throughout the pH titration experiment, the pH meter was placed into the transparent solution while swirling it. The acid with a concentration of 0.01 ᴍ was introduced into the solution. The amounts of acid applied in the two inflection points, pH values of 8.4 and 4.7, were recorded. The weight percent of LiOH and Li_2CO_3 are calculated in the following Equations 2 and 3.

$$Li2CO3\quad (wt.\%) = \frac{(V2 - V1) \times C_{HCl} \times M_{Li2CO3}}{1000 \times \{(W_{NMC} \times W_{solution})/W_{DI\ water}\}} \times 100\ (\%) \quad (2)$$

$$LiOH\quad (wt.\%) = \frac{(2 \times V1 - V2) \times C_{HCl} \times M_{LiOH}}{1000 \times \{(W_{NMC} \times W_{solution})/W_{DI\ water}\}} \times 100\ (\%) \quad (3)$$

The V1 and V2 are ml of acid used at two inflection points, in which V2 > V1; C is the concentration of HCl; W and M are weights and molecular weights of related materials.

Density Functional Theory Calculation: All the DFT calculations were performed using the Vienna Ab initio Simulation Package (VASP) with plane wave basis associated with projector augmented wave approach.[30] Exchange correlation was treated with generalized gradient approximation (GGA) in the form of Perdew—Birke—Ernzerhof (PBE) functional.[31] As in GGA + U calculations, the effective on-site Coulomb interaction parameters for Ni, Co, and Mn were set to be 6.4, 4.9, and 4.5 eV, respectively.[32] In all the calculations, the plane-wave cutoff energy was set as 500 eV, and the total energy of the system converged within 10^{-5} eV. The surface of the NMC electrode was modeled using a slab structure containing 27 transition metals (21 Ni atoms, 3 Mn atoms, and 3 Co atoms). The Li surface segregation was modeled by moving one Li atom at the subsurface layer to the surface 3b site and leaving a Li vacancy in the subsurface coating. During structural relaxation, the atomic positions of the bottom four layers were fixed, and the force acting on each atom converged to below 0.02 eV $Å^{-1}$. The structural optimization calculations used a 4 × 4 × 1 Monkhorst-Pack k-point mesh.

Molecular Dynamics Simulations: The molecular dynamics simulations were performed by using a Large-scale Atomic/Molecular Massively Parallel Simulator (LAMMPS) package.[33] The polymer consistent force field (PCFF) was used to describe both bonding and non-bonding interactions between atoms.[34] Coulombic potential was calculated using the Ewald summation method. The cutoff distance of force was set to be 10 Å. Each cellulose chain was constructed with 8 cellobiose repeating units.[35] The functional groups of CNC and CNF were not considered in MD simulations for the efficiency of simulations. The simulation cell has an orthorhombic shape. The cellulose chains were arranged in parallel along [100] direction in a layer and along [010] direction in a subsequent layer, resulting in an interlaced pattern along [001] direction and porous structure. The dimension of the porous cellulose structure was 83.2 Å in the [100] and [010] directions and ranges from 75 to 145 Å in the [001] direction, as shown in Figure S21 (Supporting Information). To model water-cellulose interaction, H_2O molecules were added into the space between the cellulose chains. Specifically, 3220 H_2O molecules were added into the cellulose with a 5 Å interlayer spacing, 6440 H_2O molecules into the cellulose with a 10 Å interlayer spacing, and 9660 H_2O molecules into the cellulose with a 15 Å interlayer spacing, ensuring a consistent H_2O density (close to liquid water density, 1 g cm^{-3}) within the interlayer space of cellulose supercells.

The MD simulation procedure is as follows. First, geometry optimization was conducted on the water-cellulose structure until the energy tolerance of 0.0001 kcal mol^{-1} and force tolerance of 0.005 kcal mol^{-1} $Å^{-1}$ were satisfied. Subsequently, the structure was equilibrated by performing a cycle of annealing simulation. During annealing, the structure was heated from 300 to 500 K and cooled back to 300 K at intervals of 40 K. Each temperature stage was held for 0.1 ps, and the total time for a cycle of annealing was 1 ps. Finally, the equilibrated water-cellulose configurations were obtained through NVT (constant particle number, volume, and temperature) MD simulations at 600 K. The positions of cellulose were fixed during the NVT simulation. Each NVT simulation had 100, 000 steps, and each step took for 1 fs. The choice of a relatively high temperature of 600 K was intended to accelerate the molecular dynamic processes.

Supporting Information

Supporting Information is available from the Wiley Online Library or from the author.

Acknowledgements

This material is based upon work supported by the U.S. Department of Energy's Office of Energy Efficiency and Renewable Energy (EERE) under the Advanced Materials and Manufacturing Technologies Office, Award Number DE-EE0009111. The authors thank Professor Xiaoyu Tang and Langqi Jin from Northeastern University and the Northeastern University Institute for Chemical Imaging of Living Systems (CILS) for the use of confocal laser scanning microscopes. The authors appreciate Dr. Ke Zhang, Priru Chen, and Jiachen Lin from Northeastern University for the use of Nano ZS Zetasizer. Y.F. and G.W. acknowledge the support from National Science Foundation (NSF CMMI 1760916). This research was also supported in part by the University of Pittsburgh Center for Research Computing through the resources provided. Specifically, this work used the H2P cluster, which is supported by NSF award number OAC-2117681. This research used the beamline 11-BM (CMS) of the National Synchrotron Light Source II, a U.S. Department of Energy (DOE) Office of Science User Facility operated for the DOE Office of Science by Brookhaven National Laboratory under Contract No. DE-SC0012704.

Conflict of Interest

The authors declare no conflict of interest.

Data Availability Statement

Research data are not shared.

Keywords

aqueous processing, environmental sustainability, nanocellulose, nickel-rich nmc, protective coating

Received: July 31, 2024
Revised: August 31, 2024
Published online:

---

[1] a) P. Teichert, G. G. Eshetu, H. Jahnke, E. Figgemeier, *Batteries* **2020**, *6*, 8; b) M. Wood, J. Li, R. E. Ruther, Z. Du, E. C. Self, H. M. Meyer III, C. Daniel, I. Belharouak, D. L. Wood III, *Energy Storage Mater.* **2020**, *24*, 188; c) M. S. Houache, C. H. Yim, Z. Karkar, Y. Abu-Lebdeh, *Batteries* **2022**, *8*, 70.
[2] L. Zou, Y. He, Z. Liu, H. Jia, J. Zhu, J. Zheng, G. Wang, X. Li, J. Xiao, J. Liu, *Nat. Commun.* **2020**, *11*, 3204.
[3] I. A. Shkrob, J. A. Gilbert, P. J. Phillips, R. Klie, R. T. Haasch, J. Bareno, D. P. Abraham, *J. Electrochem. Soc.* **2017**, *164*, A1489.
[4] a) L. Azhari, X. Zhou, B. Sousa, Z. Yang, G. Gao, Y. Wang, *ACS Appl. Mater. Interfaces* **2020**, *12*, 57963; b) I. Hamam, N. Zhang, A. Liu, M. Johnson, J. Dahn, *J. Electrochem. Soc.* **2020**, *167*, 130521.

[5] I. Doberdò, N. Löffler, N. Laszczynski, D. Cericola, N. Penazzi, S. Bodoardo, G. T. Kim, S. Passerini, *J. Power Sources* **2014**, *248*, 1000.

[6] C. Yuan, H. Cao, K. Shen, Y. Deng, D. Zeng, Y. Dong, M. Hauschild, *CIRP Ann.* **2021**, *70*, 25.

[7] a) C. Zhao, Y. Lu, K. Yan, Y. Guan, S. Jiang, J. Wang, S. Guo, M. Cao, N. Li, Y. Su, *Adv. Energy Mater.* **2024**, *14*, 2304532; b) S. Guo, Y. Su, K. Yan, C. Zhao, Y. Lu, H. Wang, J. Dong, N. Li, Y. Liu, Y. Guan, *Adv. Sci.* **2024**, *11*, 2404307.

[8] Y. Wu, Y. Li, Y. Wang, Q. Liu, Q. Chen, M. Chen, *J. Energy Chem.* **2022**, *64*, 62.

[9] Y. B. Wang, Q. Yang, X. Guo, S. Yang, A. Chen, G. J. Liang, C. Y. Zhi, *Rare Met.* **2022**, *41*, 745.

[10] S. Trivedi, V. Pamidi, S. P. Bautista, F. N. A. Shamsudin, M. Weil, P. Barpanda, D. Bresser, M. Fichtner, *Adv. Energy Mater.* **2024**, *14*, 2303338.

[11] a) N. Loeffler, G. T. Kim, F. Mueller, T. Diemant, J. K. Kim, R. J. Behm, S. Passerini, *ChemSusChem* **2016**, *9*, 1112; b) M. Memm, A. Hoffmann, M. Wohlfahrt-Mehrens, *Electrochim. Acta* **2018**, *260*, 664.

[12] W. Bauer, F. A. Çetinel, M. Müller, U. Kaufmann, *Electrochim. Acta* **2019**, *317*, 112.

[13] a) A. Kazzazi, D. Bresser, A. Birrozzi, J. von Zamory, M. Hekmatfar, S. Passerini, *ACS Appl. Mater. Interfaces* **2018**, *10*, 17214; b) S. Radloff, R. G. Scurtu, M. Hölzle, M. Wohlfahrt-Mehrens, *J. Electrochem. Soc.* **2021**, *168*, 100506; c) S. Radloff, R. G. Scurtu, M. Hölzle, M. Wohlfahrt-Mehrens, *J. Electrochem. Soc.* **2022**, *169*, 040514.

[14] Z. Du, J. Li, M. Wood, C. Mao, C. Daniel, D. L. Wood III, *Electrochim. Acta* **2018**, *270*, 54.

[15] a) H. Zhu, W. Luo, P. N. Ciesielski, Z. Fang, J. Zhu, G. Henriksson, M. E. Himmel, L. Hu, *Chem. Rev.* **2016**, *116*, 9305; b) R. Calle-Gil, E. Castillo-Martínez, J. Carretero-González, *Adv. Sustainable Syst.* **2022**, *6*, 2100395.

[16] a) J. Wang, D. J. Gardner, N. M. Stark, D. W. Bousfield, M. Tajvidi, Z. Cai, *ACS Sustainable Chem. Eng.* **2018**, *6*, 49; b) L. Wang, P. V. Kelly, N. Ozveren, X. Zhang, M. Korey, C. Chen, K. Li, S. Bhandari, H. Tekinalp, X. Zhao, *Matter* **2022**, *6*, 344.

[17] L. Solhi, V. Guccini, K. Heise, I. Solala, E. Niinivaara, W. Xu, K. Mihhels, M. Kröger, Z. Meng, J. Wohlert, *Chem. Rev.* **2023**, *123*, 1925.

[18] X. Geng, W. Sun, W. Wu, B. Chen, A. Al-Hilo, M. Benamara, H. Zhu, F. Watanabe, J. Cui, T.-p. Chen, *Nat. Commun.* **2016**, *7*, 10672.

[19] Y. Qi, Y. Guo, A. A. Liza, G. Yang, M. H. Sipponen, J. Guo, H. Li, *Cellulose* **2023**, *30*, 4115.

[20] a) T. Saito, S. Kimura, Y. Nishiyama, A. Isogai, *Biomacromolecules* **2007**, *8*, 2485; b) T. W. Kurniawan, H. Sulistyarti, B. Rumhayati, A. Sabarudin, *J. Chem.* **2023**, https://doi.org/10.1155/2023/5037027.

[21] A. Isogai, T. Saito, H. Fukuzumi, *Nanoscale* **2011**, *3*, 71.

[22] X. Geng, Y. Zhang, Y. Han, J. Li, L. Yang, M. Benamara, L. Chen, H. Zhu, *Nano Lett.* **2017**, *17*, 1825.

[23] S. J. Sim, S. H. Lee, B. S. Jin, H. S. Kim, *Sci. Rep.* **2020**, *10*, 11114.

[24] J. Gong, J. Li, J. Xu, Z. Xiang, L. Mo, *RSC Adv.* **2017**, *7*, 33486.

[25] Y. Wang, A. S. Mijailovic, T. Ji, E. Cakmak, X. Zhao, L. Huang, B. W. Sheldon, H. Zhu, *Energy Storage Mater.* **2024**, *71*, 103546.

[26] D. Bahamon, M. Khalil, A. Belabbes, Y. Alwahedi, L. F. Vega, K. Polychronopoulou, *RSC Adv.* **2021**, *11*, 2947.

[27] Z. Cheng, H. Ye, F. Cheng, H. Li, Y. Ma, Q. Zhang, A. Natan, A. Mukhopadhyay, Y. Jiao, Y. Li, *Adv. Mater. Interfaces* **2019**, *6*, 1802010.

[28] Q. Li, Y. Yin, D. Cao, Y. Wang, P. Luan, X. Sun, W. Liang, H. Zhu, *ACS Nano* **2021**, *15*, 11992.

[29] Y. Zhang, X. Sun, D. Cao, G. Gao, Z. Yang, H. Zhu, Y. Wang, *Energy Storage Mater.* **2021**, *41*, 505.

[30] a) G. Kresse, J. Furthmüller, *Phys. Rev. B* **1996**, *54*, 11169; b) G. Kresse, D. Joubert, *Phys. Rev. B* **1999**, *59*, 1758.

[31] J. P. Perdew, K. Burke, M. Ernzerhof, *Phys. Rev. Lett.* **1996**, *77*, 3865.

[32] a) H. Chen, J. A. Dawson, J. H. Harding, *J. Mater. Chem. A* **2014**, *2*, 7988; b) L. Wang, T. Maxisch, G. Ceder, *Phys. Rev. B* **2006**, *73*, 195107; c) K. Min, S. W. Seo, Y. Y. Song, H. S. Lee, E. Cho, *Phys. Chem. Chem. Phys.* **2017**, *19*, 1762.

[33] A. P. Thompson, H. M. Aktulga, R. Berger, D. S. Bolintineanu, W. M. Brown, P. S. Crozier, P. J. in't Veld, A. Kohlmeyer, S. G. Moore, T. D. Nguyen, *Comput. Phys. Commun.* **2022**, *271*, 108171.

[34] H. Sun, S. J. Mumby, J. R. Maple, A. T. Hagler, *J. Am. Chem. Soc.* **1994**, *116*, 2978.

[35] Y. Nishiyama, P. Langan, H. Chanzy, *J. Am. Chem. Soc.* **2002**, *124*, 9074.